

# A High GOPs/Slice Time Series Classifier for Portable and Embedded Biomedical Applications

Hamid Soleimani, Wilten Nicola, Claudia Clopath, Emmanuel. M. Drakakis

## Abstract

Modern wearable rehabilitation devices and health support systems operate by sensing and analysing human body activities. The information produced by such systems requires efficient methods for classification and analysis. Deep learning algorithms have shown remarkable potential regarding such analyses, however, the use of such algorithms on low-power wearable devices is challenged by resource constraints. Most of the available on-chip deep learning processors contain complex and dense hardware architectures in order to achieve the highest possible throughput. Such a trend in hardware design may not be efficient in applications where on-node computation is required and the focus is more on the area and power efficiency as in the case of portable and embedded biomedical devices. The aim of this paper is to overcome some of the limitations in a current typical deep learning framework and present a flexible and efficient platform for biomedical time series classification. Here, throughput is traded off with hardware complexity and cost exploiting resource sharing techniques. This compromise is only feasible in systems where the underlying time series is characterised by slow dynamics as in the case of physiological systems. A Long-Short-Term-Memory (LSTM) based architecture with ternary weight precision is employed and synthesized on a Xilinx FPGA. Hardware synthesis and physical implementation confirm that the proposed hardware can accurately classify hand gestures using surface-electromyographical time series data with low area and power consumption. Most notably, our classifier reaches  $1.46\times$  higher GOPs/Slice than similar state of the art FPGA-based accelerators.

## 1 Introduction

Recognizing internal activities of the human body based on biologically generated time series data is at the core of technologies used in wearable rehabilitation devices [1] and health support systems [2]. Some commercial examples include fitness trackers or fall detection devices. Wearable activity recognition systems are generally composed of sensors, such as accelerometers, gyroscopes or magnetic field/chemical sensors [3] and a processor used to analyze the generated signals. Real-time and accurate interpretation of the recorded physiological data from these devices can be considerably helpful in prevention and treatment of a number of diseases [4]. For instance, patients with diabetes, obesity or heart disease are often required to be closely monitored and follow a specific exercise set as part of their treatments [5]. Similarly, patients with mental pathologies such as epilepsy can be monitored to detect abnormal activities and therefore prevent negative consequences [6].

However, most current commercial products only offer relatively simple metrics, such as step count or heart beat. Further, they lack the complexity and computing power for many time series classification problems of interest in real time. The emergence of deep learning methodologies capable of learning multiple layers of feature hierarchies and temporal dependencies in time series problems and increased processing capabilities in wearable technologies lay the ground work to perform more detailed data analysis on-node and in real time. The ability to perform more complex analysis, such as human activity classification, on the wearable device/node could potentially relax the burden of data streaming from the device to host and thus save data bandwidth link. This bandwidth saving is more visible in the cases where the classification task should be continuously performed on the patient such as in seizure detection for epileptic patients or continuous imaging and classification of bladder, liver and heart using ultrasound machines. However, due to the high computational power and memory bandwidth required by deep learning algorithms, full realization of such systems on wearable and embedded medical devices is still challenging.

On the other hand, the recent development focus of deep learning hardware accelerators has been mainly on achieving the highest possible throughput. This is to keep up with the real-time requirements of complex and embedded machine learning algorithms. In such systems, a large number of Multiply Accumulate (MAC) processors are embedded into the architecture in order to achieve the highest possible throughput. Such strategies in hardware design would lead to large area ( $\sim 600\text{ mm}^2$ ) and power ( $\sim 500\text{ W}$ ) requirements [7] [8] [9]. In this paper we propose an alternative approach based on the observation that most physiological time series are slow, ranging between 0–500 Hz. In such systems, since the real-time classification rate is low, the throughput can be traded off with hardware complexity using resource sharing techniques. Therefore, we introduce a low cost time series classifier based on Long-Short-Term-Memory (LSTM) [10] networks which is ideally suited for portable

and embedded biomedical applications. As a case study, we examine the performance of the proposed hardware on a hand gesture database [11] recorded by instantaneous surface electromyography (sEMG). Furthermore, as in the case of deep-networks, our hardware classifier can be also applied to post-feature extraction.

The rest of the paper is organized as follows: in Section 2, the proposed hardware-oriented classifier is described in detail, while in Section 3, the performance of the classifier when sweeping free parameters is measured on a synthetic database. Sections 4 and 5 investigate high level and detailed structure of the proposed hardware classifier respectively. FPGA implementation results are presented in Section 6 and the proposed classifier is applied to a biomedical case study in Section 7.

## 2 Hardware-oriented Time-series Classifier

LSTM networks are very powerful Recurrent Neural Networks (RNN) that explicitly add memory gates [10]. This makes the training procedure more stable and allows the model to conveniently learn both long and short-term dependencies. There are some variations on the LSTM architecture, however in this paper we use the following model [12]:

$$\begin{cases} \mathbf{h}_{n+1}^f = \sigma(\mathbf{W}_f^T \cdot \mathbf{x}_n + \mathbf{b}_f) \\ \mathbf{h}_{n+1}^i = \sigma(\mathbf{W}_i^T \cdot \mathbf{x}_n + \mathbf{b}_i) \\ \mathbf{h}_{n+1}^o = \sigma(\mathbf{W}_o^T \cdot \mathbf{x}_n + \mathbf{b}_o) \\ \mathbf{h}_{n+1}^c = \tanh(\mathbf{W}_c^T \cdot \mathbf{x}_n + \mathbf{b}_c) \\ \mathbf{c}_{n+1} = \mathbf{h}_n^f \circ \mathbf{c}_n + \mathbf{h}_n^i \circ \mathbf{h}_n^c; \\ \mathbf{h}_{n+1} = \mathbf{h}_n^o \circ \tanh(\mathbf{c}_{n+1}); \\ \mathbf{y}_{n+1} = \mathbf{W}^T \mathbf{h}_n + \mathbf{b}_y \end{cases} \quad (1)$$

where  $\mathbf{x}_n = [\mathbf{h}_n, \mathbf{u}_n]$  and  $\mathbf{u}_n$ ,  $\mathbf{h}_n$  and  $\mathbf{c}_n$  are the input, output and cell state vectors respectively at discrete time index,  $n$ . The operator  $\circ$  denotes the Hadamard element by element product. The variables  $\mathbf{h}_n^f$ ,  $\mathbf{h}_n^i$ ,  $\mathbf{h}_n^o$  represent the forgetting, input and output gating vectors. The parameter  $\mathbf{y}_n$  is a fully connected layer following the LSTM block and serves as the network output and its size is determined by the number of output classes and as well as the number of hidden neurons. Finally,  $\mathbf{W}_f$ ,  $\mathbf{W}_i$ ,  $\mathbf{W}_o$ ,  $\mathbf{W}_c$ ,  $\mathbf{W}_y$  and  $\mathbf{b}_f$ ,  $\mathbf{b}_i$ ,  $\mathbf{b}_o$ ,  $\mathbf{b}_c$ ,  $\mathbf{b}_y$  are the weights and biases for the different layers, respectively.

One of the main bottlenecks for the hardware realization of RNNs and convolutional neural networks (CNNs) is the large memory size and bandwidth required to fetch weights in each operation. To alleviate the need for such high bandwidth memory access, we investigate two quantization methods (binary and ternary) introduced in [13] [14] to quantize weights embedded in the network architecture. As the changes during gradient descent are small, it is important to maintain sufficient resolution otherwise no change is seen during the training process, therefore the real-valued gradients of weights are accumulated in real-valued variables. We also set the bias values to zero to achieve further efficiency in hardware realization while delivering an acceptable classification accuracy for the experimented biomedical case study. Such quantization methods can be considered as a form of regularization that can help the network to generalize. In particular, the binary and ternary quantization are a variant of Dropout, in which weights are binarized/ternarized instead of randomly setting part of the activations to zero when computing the parameter gradients [13].

The quantization of weights in the forward path must be also reflected in the calculation of the gradient descent. Here, we use the version of the straight-through estimator introduced in [13] that takes into account the saturation effect. Consider the sign and round functions for binary and ternary quantization respectively as follows:

$$\begin{cases} q_b = \text{sign}(r) \\ q_t = \text{round}(r) \end{cases} \quad (2)$$

where  $r = W_x$  and assume that estimators  $g_{q_b}$  and  $g_{q_t}$  of the gradients  $\frac{\delta C}{\delta q_b}$  and  $\frac{\delta C}{\delta q_t}$  ( $C$  is the cost function) are derived. Then, the straight-through estimators of  $\frac{\delta C}{\delta r}$  are:

$$\begin{cases} g_{r_b} = g_{q_b} 1_{|r| \leq 1} \\ g_{r_t} = g_{q_t} 1_{|r| \leq 1} \end{cases} \quad (3)$$

This implies that the gradient is applied to the weights if their real values are between 1 and -1 otherwise the gradient is cancelled when  $r$  is outside the range. The overall architecture of the proposed LSTM-based classifier is shown in Fig. 1. In this approach, the sequential target replication technique inspired from [15] is used during the training phase. However our approach is slightly different. In the proposed architecture, during forward path and for all *steps*, the same output label is used to calculate the output error. The error is stored  $s$  times in memory in order to calculate the gradient descent during the backward path. In the backward pass,

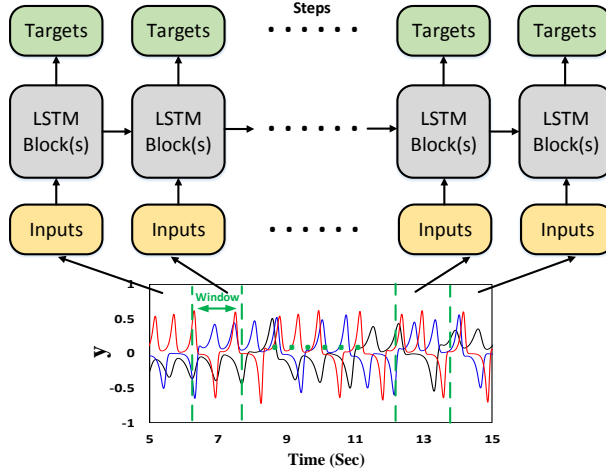


Figure 1: The overall architecture of the proposed LSTM-based classifier along with three input synthetic time series reproduced by the Lorenz attractor dynamical systems. A portion of the input signal termed as *window* is highlighted in green color, sequentially fed to the systems after *steps* times.

the RNN is unrolled back in time and the weights are updated. This technique forces the network to better memorize the previous sequences of the input windows [16]. It should be also noted that during the training phase loss values are averaged over all steps, while at the inference (test) time, the output at the final step is chosen as the actual classification value.

### 3 Hardware-oriented Simulations

In order to measure the performance of each quantization method, we synthetically produce and classify a number of time series as a preliminary proof of principle. In this example, we generate synthetic time series data from well known chaotic dynamical systems in different parameter regimes. In all parameter regimes, these systems have chaotic attractors. The unique and isolated parameter regime corresponds to discrete classes. The LSTM network is tasked to classify the resulting time series as belonging to a unique class. The considered dynamical systems are the logistic (discrete time) and Lorenz systems (continuous time). The logistic map is given by:

$$x_{n+1} = r \cdot x_n(1 - x_n)$$

where  $x$  is the state variable and  $r$  is a parameter [17]. The Lorenz system is given by:

$$\begin{aligned} \dot{x} &= \sigma(y - x) \\ \dot{y} &= x(\rho - z) - y \\ \dot{z} &= xy - \beta z \end{aligned}$$

where  $x$ ,  $y$  and  $z$  are state variables and  $\sigma$ ,  $\rho$ ,  $\beta$  are parameters [18].

By sweeping  $r$  in the Logistic map and  $\sigma$  in the Lorenz attractor, various responses can be observed (Figure 2A). The time series data generated by the chaotic dynamical systems must be similar between the classes in terms of both time and frequency features so that the signals are not easily distinguishable by the classifier. To determine how similar the synthetic data classes are and visualize our synthetic data set in a simple way, we computed a distance matrix in the Fourier domain as

$$D(i, j) = \int_{\omega} (|P_i(\omega)| - |P_j(\omega)|)^2 d\omega \quad (4)$$

where  $P(\omega)$  is the logarithm of the power of the Fourier transforms of  $\frac{x_i(t)}{20}$ , for  $i = 1, 2, \dots, N_S$  realizations for a sample of  $N_S = 100$  realizations per discrete parameter class. The factor of  $1/20$  multiplying  $x_i(t)$  bounds the trajectories in the unit interval for subsequent learning in the LSTM network. Then, we looked for a set of points in  $\mathbb{R}^2$ ,  $(x_i, y_i)$  (Figure 2B) such that

$$\hat{D}(i, j) = (x_i - x_j)^2 - (y_i - y_j)^2$$

by stochastically minimizing the sum:

$$E = \sum_{i \neq j} \left( \hat{D}(i, j) - D(i, j) \right)^2$$

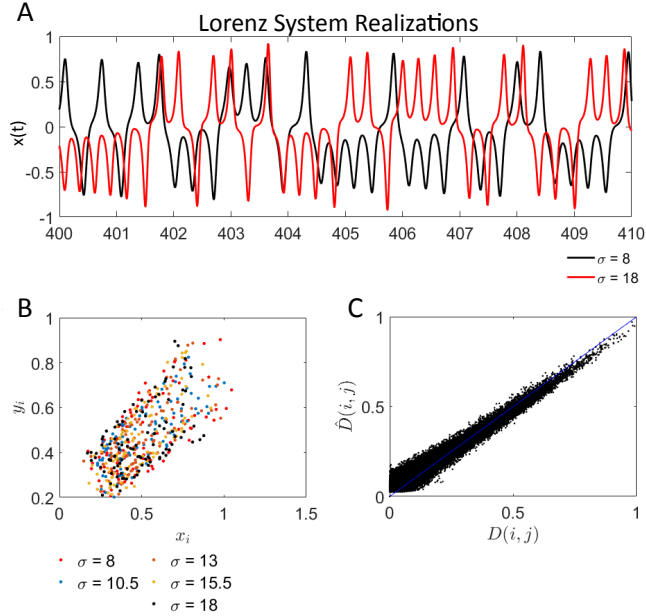


Figure 2: (A) A realization of the Lorenz system for  $\sigma = 8$  (red) and  $\sigma = 18$  (black). The other parameters were taken to be  $\rho = 28$  and  $\beta = \frac{5}{3}$ . The  $x(t)$  variable is plotted, downsampled by a factor of 40 such that it is bounded in the interval  $[-1, 1]$  for subsequent network training. (B) The final  $(x_i, y_i)$  generated by the Fourier Spectrum and the visualization procedure outlined in the text. The data displays no clear clustering in the Fourier domain with a 2-dimensional projection for the 5 classes considered. (C) A plot of  $\hat{D}(i, j)$  vs  $D(i, j)$ . The computed correlation coefficient for the Lorenz data was  $p = 0.9826$ , indicating that the Fourier domain data is well described as lying on a 2-D manifold.

This approach finds low dimensional (in this case 2D) manifolds that the data may lie on. Alternatively, one may also use the singular value decomposition, however we do not take that approach here. The stochastic minimization occurs by initializing the  $(x_i, y_i)$  from a joint uniform distribution on  $[0, 1]^2$ , randomly perturbing every point to compute  $E$ . The perturbations were drawn from a normal distribution with mean 0 and standard deviation  $\eta = 10^{-3}$ . At each time step, the network computes  $E$  after  $(x_i, y_i)$  have been perturbed and compares  $E$  to the smallest value of  $E$  so far,  $E^*$ . If  $E < E^*$ , then we set the new  $E^* = E$  and keep the perturbed  $(x_i, y_i)$ . If  $E^* < E$ , we disregard the perturbation and iterate. The results of this process are shown in Fig. 2A-C for the Lorenz system without noise. The results demonstrate that the data has no readily visible clusters in a 2-dimensional projection, however clustering may appear in a higher dimensional projection. In order for the network to generalize the input features better, a uniform random noise is added to the training and test data. Since binarization is a form of regularization [14], we do not use other regularization methods such as Dropout. All weights are initialized by random numbers with normal distribution. The same analysis applied to the Logistic map showed that the generated time series are separable in the Fourier domain, however still difficult to visually classify in the time domain.

To compare the performance of the network with different weight precision, experiments with different free parameters were performed on the database. The free parameters are defined as follows:

- Window ( $\omega_s$ ): the length of each part of the input time series fed to the network to be classified in the output. The length of input signal ( $\mathbf{u}$ ) is equal to  $M \cdot \omega_s$  where  $M$  is the dimension of the input signal. For example,  $M$  for data collected from a three dimensional gyroscope is 3 as the input signal is presented to the system by 3 independent time series. A highlighted window sample is shown in Fig. 1.
- Iteration ( $s$ ): the number of successive windows that must be introduced to the network sequentially so that the network can classify the input signals properly. The partition of the input signals into window sizes and then introducing them to the network sequentially would allow the RNNs to use recurrent feedback and internal memories to make decisions, leading to a significant reduction in hardware area consumption.
- Output Class ( $N_y$ ): the number of classes that the network must classify based on the input signals. We can specify this by considering more discrete parameter sets in our chaotic systems.
- Hidden neurons ( $N_h$ ): the number of neurons embedded in the network. Accuracy increases with the number of hidden neurons at the expense of higher hardware cost. After a certain point, there are diminishing returns in increasing the number of hidden neurons.

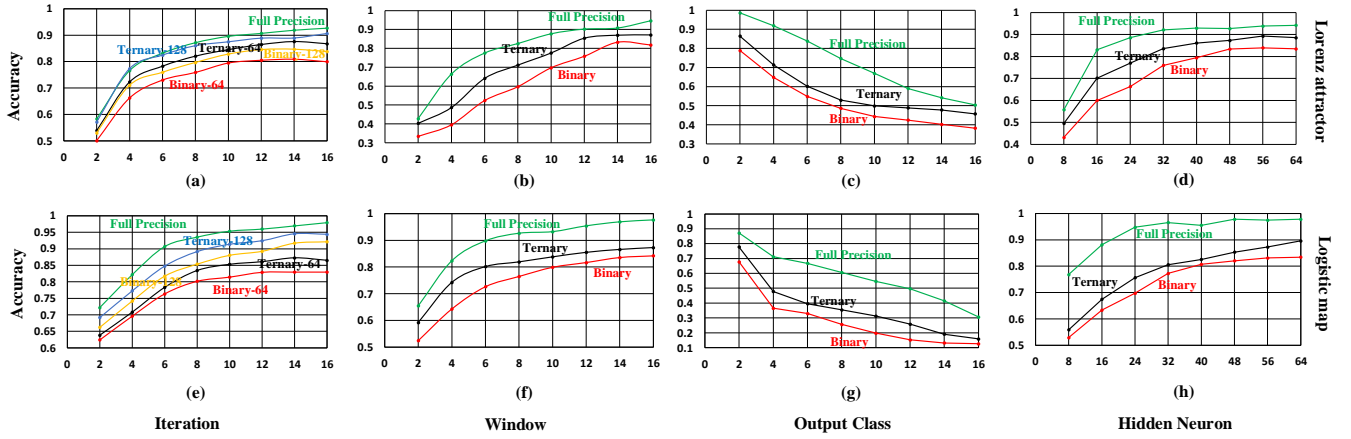


Figure 3: Free parameter sweeping for three networks with various weight precision on two synthetic database extracted from Lorenz (a–d) and logistic map (e–h). The networks’ accuracies are changed by varying *iteration* in (a) and (e), *window* size in (b) and (f), *output class* in (c) and (g) and *hidden neuron* in (d) and (h). In addition, two sets of binary and ternary networks are compared in (a) and (e).

In these experiments, the LSTM network takes a sequence of continuous/discrete arrays defined by the  $\omega_s$  size as input, and after  $s$  steps classifies it into one of the output classes. The training objective (loss function) is the cross-entropy loss over all target sequences as follows:

$$L_i = -\log(p_{y_i}); p_k = \frac{e^{y_k}}{\sum_j e^{y_j}} \quad (5)$$

where  $k$  is the array of class scores for a single example and  $p$  is a vector of the output normalised probabilities. In order to backpropagate the output error to all layers,  $\frac{\delta L_i}{\delta f_k}$  can be derived using chain rule as follows:

$$\frac{\delta L_i}{\delta f_k} = p_k - 1(y_i = k). \quad (6)$$

Adagrad is used as the learning algorithm with learning rate of  $5e-2$  [19]. The weights are randomly drawn from a uniform distribution in  $[-0.01, 0.01]$ . After each iteration, the gradients are clipped to the range  $[-5, 5]$ . The results of sweeping on the free parameters of the test synthetic database for the binary, ternary and full precision networks are shown in Fig. 3. As can be seen in Fig. 3 (a) and (e), by increasing  $s$ , the accuracy of the classifier increases at the expense of longer latency and higher power consumption for the hardware realization. It can be also observed that the quantized networks with the same number of neurons (64) can classify the input signals with a lower accuracy rate. However, this reduction in the accuracy can be compensated by increasing the number of hidden neurons. For example, 128 neurons in the quantized network have similar performance compared to 64 neurons in a full precision network. Although requiring more neurons in a quantized network, a significant hardware efficiency improvement can be still seen. It is also observed that the ternary network possesses better accuracy performance compared to its binarized counterpart thereby confirming the results in [14].

The effect of varying window size  $\omega_s$  on the accuracy for all networks are shown in Fig. 3 (b) and (f). Increasing  $\omega_s$ , increases the accuracy for all networks but this imposes a higher hardware cost in terms of area and power. Thus, by increasing the length of the scanned input signals, the number of operations and the memory bandwidth per input increase. Moreover, these plots show that the accuracy drops as quantization is applied to the weights. Again, this reduction in accuracy can be compensated by increasing the number of hidden neurons while still achieving better hardware area performance compared to the full precision.

Fig. 3 (c) and (g) show that the accuracy of the classifier drops in all networks if the number of output classes increases. However, similar to the previous experiments this reduction in accuracy can be compensated up to a certain point by increasing the number of hidden neurons as observed in Fig. 3 (d) and (h).

## 4 Finite State Machine

As illustrated in Fig. 4, the proposed hardware classifier functions as a finite state machine that iterates through six states and only one state is active at a time. This structure can also be implemented in a pipelined form with multiple active states and higher throughput at the expense of increased power and area consumption. The general functionality of each state is briefly described as follows:

**State 1:** After initialization at the start state, the first input transmission according to the defined  $\omega_s$  is carried out and the system enters the first state where  $\mathbf{W}_f^T \mathbf{x}_1$ ,  $\mathbf{W}_i^T \mathbf{x}_1$ ,  $\mathbf{W}_o^T \mathbf{x}_1$  and  $\mathbf{W}_c^T \mathbf{x}_1$  are independently

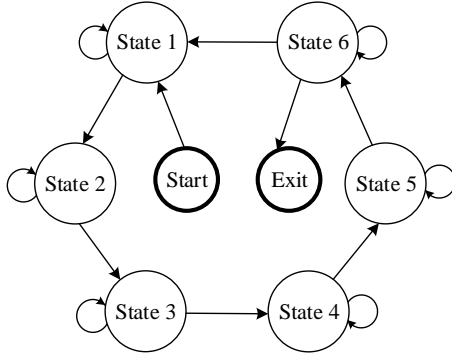


Figure 4: Finite state machine block diagram for the proposed hardware architecture. The system iterates through six states and only one state is active at a time.

calculated each with eight additions per clock cycle. A total of  $[N_h + \omega_s] \times \frac{N_h}{8}$  clock pulses are needed for this state to finish the calculations.

**State 2:** At the end of the calculations, the system enters the second state. In this state, according to (1), nonlinear functions ( $\sigma(\cdot)$  and  $\tanh(\cdot)$ ) are applied to the previous values fetched from memories. After  $N_h$  clock pulses, the system enters the next state.

**State 3:** In this state, using two embedded multipliers, the value of variable  $c$  is calculated in  $N_h$  clock pulses. The critical path of the proposed architecture is limited by this state which can be alleviated by using pipelined or serial multipliers at the expense of increased latency and hardware cost.

**State 4:** As the variable  $c$  is provided, the system enters this state where the  $\tanh(\cdot)$  function is applied to the previous values, taking  $N_h$  clock pulses, then the system enters the next state.

**State 5:** In this state, using one of the two embedded multipliers, the value of variable  $h$  is calculated in  $N_h$  clock pulses and the system enters the next state.

**State 6:** Finally, if the number of scan times is equal to  $s$ , by calculating  $\mathbf{W}_y^T \mathbf{h}$  in  $N_h \times N_y$  clock pulses, the system determines the classified output and exits, otherwise enters State 1. This process is repeated for each window of the input signal(s) and managed by a master controller circuit, embedded into the system.

## 5 Hardware Architecture

As stated before, the aim of this paper is to present a flexible and efficient hardware-based time series classifier that exploits the slow nature of physiological signals for reducing hardware complexity and cost. In such systems, given that the classification rate is low, a few high speed processor modules are enough to share the computational burden in different layers. This would also allow us to actively and efficiently reconfigure the system according to the user's specifications for the set number of neurons, window size, iterations and input/output classes. The architecture of the proposed system is shown in Fig. 5 in which the hardware modules (maximum 64 operations per clock cycle) are shared through a 96-bit bus. It should be stressed that since the accuracy of the ternary network is generally higher than its binary counterpart as shown in Fig. 3, in the hardware implementation, the ternary quantization is used and two bits are allocated for storing each weight value. In the following, the architecture of each hardware module is explained in detail:

**WBs (Weight Banks):** This block contains five sets of buffers to store the truncated 2-bit weights ( $\omega_f$ ,  $\omega_i$ ,  $\omega_o$ ,  $\omega_c$ , and  $\omega_y$ ), trained off-line. The *WBs* module is able to read maximum 64 bits in each clock cycle. The utilised volume of each buffer is defined by the user which is equal to  $2N_h(N_h + \omega_s)$  bits. However, the maximum volume of these buffers must be selected based on the available resources on the chip. The greater the volume size, the wider the range of flexibilities for the network/input size. The reading process of this block is controlled by the *MC* unit and the block is only activated upon its use. It should be noted that, as the proposed architecture is implemented on a Xilinx FPGA in this work, the buffers are realised using block RAMs and the address of each reading operation is provided on the negative clock edge by the *MC* module. This module is used only in states 1 and 6 of the FSM.

**IMs (Internal Memories):** This block contains seven sets of buffers to store 12-bit values produced by the intermediate stages ( $\mathbf{h}_f$ ,  $\mathbf{h}_i$ ,  $\mathbf{h}_o$ ,  $\mathbf{h}_c$ ,  $\mathbf{h}$ ,  $\mathbf{c}$ , and  $\mathbf{y}$ ). The maximum and utilised volume of the buffers are again determined by the available on-chip memory and the user's specifications respectively. The writing and reading of this block is also controlled by the *MC* unit and the reading address is provided on the negative clock edge as they are implemented using block RAMs. The maximum data bandwidth of this module is utilised in states 1, 2 and 3 which is 48 bits and the module is active in all states.

**MAC1s (Multiply-Accumulate [limited precision]):** This blocks contains 32 parallel MAC units with limited precision. Each unit computes the product of 12 and 2-bit signed numbers and adds the product to an accumulator. The number of iterations that this unit needs to operate is defined by the user and assigned

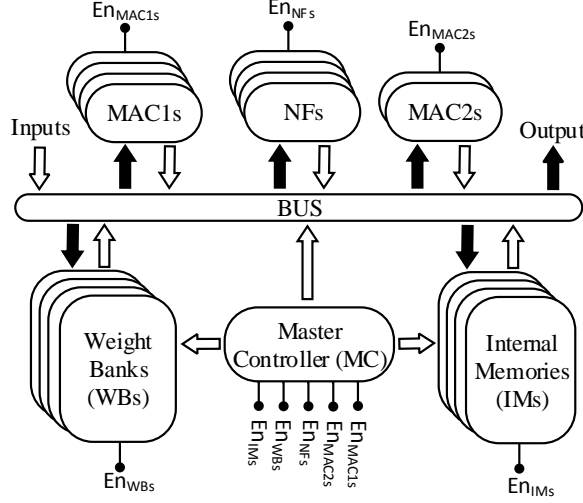


Figure 5: The proposed architecture of the system comprising six blocks: MAC1s, NFs, MAC2s, WBs, IMs and MC. Black and white arrows represent output and input signals respectively in accordance with bus connections

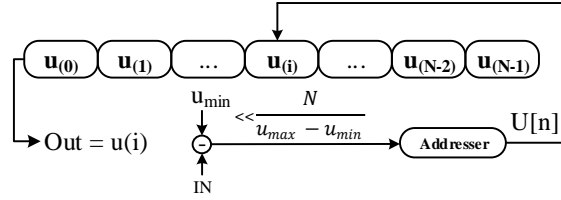


Figure 6: The look-up table based architecture of NFs. In each use, according to the input value, the corresponding address ( $U[n]$ ) is generated and output value ( $u[i]$ ) is fetched from the memory.

by the *MC* block. In state 1, the  $k$ th value of each intermediate stage is calculated as follows:

$$\begin{cases} h_{f_k} = \sum_{j=1}^{(N_h+\omega_s)/z} \sum_{i=1}^z \mathbf{x}_{ss(j-1)\times z+i} \times \omega_{f_k,(j-1)\times z+i} \\ h_{i_k} = \sum_{j=1}^{(N_h+\omega_s)/z} \sum_{i=1}^z \mathbf{x}_{ss(j-1)\times z+i} \times \omega_{i_k,(j-1)\times z+i} \\ h_{o_k} = \sum_{j=1}^{(N_h+\omega_s)/z} \sum_{i=1}^z \mathbf{x}_{ss(j-1)\times z+i} \times \omega_{o_k,(j-1)\times z+i} \\ h_{c_k} = \sum_{j=1}^{(N_h+\omega_s)/z} \sum_{i=1}^z \mathbf{x}_{ss(j-1)\times z+i} \times \omega_{c_k,(j-1)\times z+i} \end{cases} \quad (7)$$

The 32 MAC units calculate the internal sum of  $z = 8$  for each intermediate stage in parallel. Moreover, the  $p$ th output value is calculated by means of this block in state 6 as follows:

$$y_{s_p} = \sum_{j=1}^{N_h} h_j \times \omega_{y_p,j}. \quad (8)$$

It should be stressed that since the weight values are truncated to 2-bit precision  $(-1,0,1)$ , the multiplications in this block are simply implemented by multiplexers.

**MAC2s (Multiply–Accumulate [full precision])** : Two signed multipliers and a 12-bit adder are embedded in this block and used in states 3 and 5. This module acts as a MAC processor in state 3 and is reset in each cycle. This means that, the two multipliers and the adder are used in a normal operation not necessarily as MACs. In this state, the  $k$ th value of variable  $c$  is sequentially calculated as follows:

$$c_k = (h_f)_k \cdot c_k + (h_i)_k \cdot (h_c)_k. \quad (9)$$

In state 5, the multipliers are only used and the  $k$ th value of the variable  $c$  is sequentially calculated as follows:

$$h_k = (h_o)_k \cdot \tanh(c_k). \quad (10)$$

**NFs (Nonlinear Functions)** : This block is responsible for the calculation of nonlinear functions ( $\sigma(u)$  and  $\tanh(u)$ ) employed in states 2 and 4 where  $u$  is the input value of these functions. As shown in Fig. 6, we store  $N$  discrete values of each nonlinear function in look-up tables with 10-bit length. The quantity  $u[i]$  is the  $i$ th stored value where  $i \in \mathbf{N} \equiv 0, 1, \dots, N - 1$ . The address of each stored value is defined as:

$$U[n] = \lfloor \frac{u - u_{min}}{\Delta u} \rfloor \quad ; \quad u \in [u_{min}, u_{max}] \quad (11)$$

Table 1: Performance comparison between the proposed system, implemented the Kintex-7 (XC7K325T) FPGA and other state of the art hardware.

	2015[20]	2016[21]	2016[22]	2017[23]	This Work
<b>Precision</b>	32bits float	32bits float	16bits float	binary	12bits fixed
<b>Frequency</b>	100 MHz	100 MHz	150 MHz	150 MHz	100 MHz
<b>FPGA Chip</b>	VX485T	VX485T	XC7Z045	ZU9EG	XC7K325T
<b>GOPs</b>	61.6	84.2	187.8	460.8	6.3
<b>Slice</b>	75123	75924	52458	47950	447
<b>GOPs/Slice</b>	8.12E-04	11.09E-04	35.8E-04	96.1E-04	141.0E-4

Table 2: Classification test error rates of the LSTM networks with different weight resolutions/structure and the hardware results trained on the DB-a with 8 output classes.

Model	Learning Rate	$N_h$	Input Window	Steps	Loss	Accuracy %
Full precision	0.05	150	10	15	0.01	97.63
Full precision	<b>0.05</b>	<b>150</b>	<b>5</b>	<b>30</b>	<b>0.01</b>	<b>97.73</b>
Ternary	0.1	250	5	30	0.08	96.41
Hardware	0.1	250	5	30	0.09	95.71

where  $\Delta u = \frac{u_{max} - u_{min}}{N}$ . If the  $u_{max}$  and  $u_{min}$  parameters are orders of 2, the division in (12) can be easily performed by arithmetic shifts. Therefore, the values of these parameters are respectively chosen to be 8 and -8 for  $\sigma(\cdot)$  function and 4 and -4 for  $\tanh(\cdot)$  function. According to (12), by preparing the address, the corresponding output value can be fetched in one clock pulse from the look-up table. In our experimental setup, the value of  $N$  is considered to be 64, providing enough accuracy for the calculation of nonlinear functions.

**MC (Master Controller)** : According to the defined parameters by the user, this block manages and controls all resources used in the architecture through a shared bus and controlling signals ( $En_{MAC1s}$ ,  $En_{MAC2s}$ ,  $En_{NFSs}$ ,  $En_{IMS}$  and  $En_{WBS}$ ). In other words, this block actively changes the state of the FSM by assigning proper tasks to the hardware modules and actively turning off the unused modules. For example, in state 1, the  $MAC1s$  and  $WBS$  modules are only active and others are deactivated. This block also controls the input and output transmissions as required. For example, the input/output ports do not update the new values unless the number of iterations is equal to *steps*.

## 6 Hardware Results

To verify the validity of the proposed hardware classifier, the architecture designed in the previous section is implemented on a Genesys 2 development system, which provides a high performance Kintex-7 (XC7K325T) FPGA surrounded by a comprehensive collection of peripheral components. The device utilization for the implementation of the proposed hardware is summarized in Table 1 along with other state of the art implementations. The focus of all other implementations is mainly on the hardware realization of CNNs; however, as the nature of computations in all deep learning algorithms is the same, for the sake of comparison the implementation results of those studies are included here. The results of hardware implementations show that the proposed classifier reaches  $1.46\times$  higher GOPs/Slice than similar state of the art FPGA-based accelerators. Obviously, less power consumption is also achieved as the number of FPGA slices used in the proposed system is lower than in other state of art hardware. Such a trade off constrains the GOPs factor, which is not critical for most slow biomedical applications. It should be also stressed that the proposed hardware is fully reconfigurable in terms of defined free parameters introduced in Section 2 and only implemented once and reprogrammed for all other cases. The proposed hardware architecture can only implement the networks with single layer LSTM, however, it can be conveniently extended for multilayer LSTM structures by modifying the **MC** module and increasing the memory volume. The required response time of the system must be seriously considered upon such modifications. For example, by adding another layer to the current design, the amount of calculations is almost doubled, therefore, the number of parallel MAC processors in the **MAC1s** module must be doubled to keep the response time of the systems constant.



Table 3: Classification test error rates of the LSTM networks with different weight resolutions/structure and the hardware results trained on the DB-c with 12 output classes.

Model	Learning Rate	$N_h$	Input Window	Steps	Loss	Accuracy %
Full precision	0.05	250	15	10	0.06	95.47
Full precision	<b>0.05</b>	<b>250</b>	<b>10</b>	<b>15</b>	<b>0.04</b>	<b>95.85</b>
Ternary	0.1	350	10	15	0.12	94.52
Hardware	0.1	350	10	15	0.14	93.83

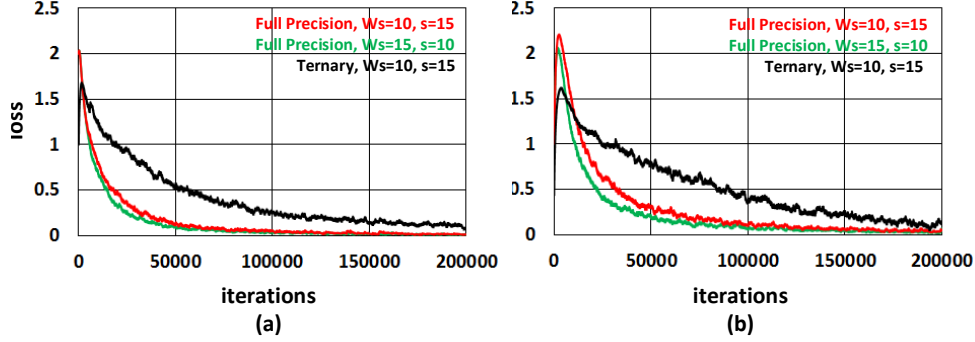


Figure 7: Training loss traces for various network structures on (a) DB-a and (b) DB-c experiment. It is evident that the ternary network converges to its final value slower than full precision networks.

## 7 Biomedical Case Study

To test the proposed architecture, we use CapgMyo [11], a hand gesture time-series database recorded by instantaneous surface electromyography (sEMG). The data was collected by a non-invasive wearable device consisting of 8 acquisition modules. Each module contained a matrix-type ( $2 \times 8$ ) electrode array with an inter-electrode horizontal distance of 7.5 mm and a vertical distance of 10.05 mm. The 128 sEMG time-series were band-pass filtered at 20-380 Hz and sampled at 1,000 Hz with a 16-bit ADC conversion. Two different experiments were tested. In experiment 1, each one of 18 subjects performed 8 basic isometric and isotonic hand gestures including *thumb up*, *extension of index and middle*, *flexion of the others*, *flexion of ring and little finger*, *extension of the others*, *thumb opposing base of little finger*, *abduction of all fingers*, *fingers flexed together in fist*, *pointing index* and *adduction of extended fingers*. The result of this experiment is termed as DB-a in the database. In experiment 2, each of the 10 subjects performed 12 gestures performed the maximal voluntary contraction (MVC) force hand gestures including *index flexion*, *index extension*, *middle flexion*, *middle extension*, *ring flexion*, *ring extension*, *little finger flexion*, *little finger extension*, *thumb adduction*, *thumb abduction*, *thumb flexion*, *thumb extension*. The result of this experiment is termed as DB-c in the database.

First, we aim at evaluating the system by classifying the DB-a actions. Therefore, the output classes are separated into 8 different actions, and the envelope of the EMG signals (using a Hilbert Transform) are extracted and applied to the networks as inputs. The classification training loss and test accuracy rates of various networks with different sizes along with hardware results are shown in Table 2. The table shows that the hardware classification rate obtained from the proposed structure is similar to the performance in [11]. It should be noted that 150 frames, (equivalent to 150 ms) is the window size suggested by several studies of pattern recognition based prosthetic control [11]. Therefore various options for  $s$  and  $\omega_s$  can be considered while the multiplication of both these parameters should be no more than 150. As  $q \cdot \omega_s$  is the latency of the system to make the final classification decision, the hardware can be efficiently used if  $\omega_s$  takes the lowest possible value while keeping  $q \cdot \omega_s$  fixed by increasing  $s$ . In this case, the network with  $\omega_s$  of 10 is chosen to be implemented on hardware. Similar experiments are performed on DB-c actions and results are reported in Table 3, however the classification rate of this network is not reported in [11]. Here, again the network architecture with narrower length of input is chosen to be implemented on hardware. Results from both tables show that the proposed hardware can achieve an accuracy comparable with a full precision network with about 40% and 30% more neurons respectively for DB-a and DB-c experiments. Although the number of neurons in the quantized ternary networks is higher than in the full precision ones, a significant hardware efficiency improvement is still seen in the quantized networks. Training loss traces for both experiments with different network structures are shown in Fig.7. Results show that the loss function in the ternary network reaches to the required minimum value, albeit slower than the full precision networks in both DB-a and DB-c experiments. Note that, this would only create delay in the training phase which is not critical as the network is trained once

Table 4: Confusion Matrix for DB-a database with 128 input time series and 8 output classes.

Output Class	Target Class							
	1	2	3	4	5	6	7	8
1	<b>98.91</b>	0.03	0.02	0.01	0	0.43	0.01	0.07
2	0.15	<b>96.47</b>	1.02	2.05	0.01	0	0.01	0.27
3	0.14	0.79	<b>97.80</b>	0.34	0.53	0	0.02	0.34
4	0	0.57	0.04	<b>95.60</b>	0.52	0	0.26	2.98
5	0	0.39	0.30	2.68	<b>94.71</b>	0	0.33	1.57
6	0.34	0	0.02	0	0.04	<b>99.32</b>	0.26	0
7	0.01	0.10	0.09	0	0.02	0.36	<b>99.31</b>	0.08
8	0	0.07	0.06	0.79	0.02	0.14	0.15	<b>98.73</b>

Table 5: Confusion Matrix for DB-c database with 128 input time series and 12 output classes.

Output Class	Target Class											
	1	2	3	4	5	6	7	8	9	10	11	12
1	<b>95.56</b>	1.09	0.37	0.96	0.30	0.24	0.23	0	0.91	0.14	0.02	0.14
2	0.68	<b>95.15</b>	0.49	0.53	0.03	0	0.11	0.16	1.36	0.96	0.18	0.24
3	0.66	0.08	<b>97.38</b>	0	0.41	0.85	0.30	0.18	0.08	0	0.01	0
4	0.09	0	0	<b>99.01</b>	0.26	0.09	0.21	0	0.27	0.01	0.03	0
5	0.01	0.26	0.31	0.44	<b>98.26</b>	0.04	0.05	0	0.02	0.36	0.19	0
6	0.02	0.01	0	0.39	0	<b>96.17</b>	3.04	0.01	0.20	0	0.11	0.01
7	0	0.29	0	0.54	0	1.89	<b>96.37</b>	0	0.76	0.12	0.01	0
8	0.08	0	0.01	0	0	0.35	0.01	<b>99.50</b>	0.03	0.01	0	0
9	0.03	0.07	0.01	0.01	0	0.07	0.15	0.32	<b>97.65</b>	0.25	0.53	0.14
10	0.09	0.18	0	0.02	0	0.18	0.05	0.01	7.07	<b>89.94</b>	1.21	1.21
11	0.20	0.19	0.01	0.39	0.11	2.81	0.79	0.02	2.95	0.60	<b>91.48</b>	0.41
12	0.37	0.51	0.01	0	.01	0.07	0.34	0.11	0.88	1.71	2.47	<b>93.49</b>

for every application.

Considering the sampling rate of 1000 Hz and according to  $\omega_s, \frac{1}{1000} \times 10 = 10 \text{ ms}$  per input window is the required response time for the system in order to operate in real-time. According to Table. II, the required operations per input window for the DB-a experiment is  $(5 \times 128 + 250) \times 250 \approx 220 \text{ K}$  operations which can be delivered in  $\sim 35 \mu\text{s}$  by the hardware classifier and is negligible compared to the required response time (10 ms). These operations may take longer for the DB-c experiment as more neurons are embedded in the network. According to Table. III, the required operations per input window for the DB-c experiment is  $(10 \times 128 + 350) \times 350 \approx 570 \text{ K}$  operations which can be delivered in  $\sim 90 \mu\text{s}$  by the hardware classifier and again is negligible compared to the required response time (10 ms).

The confusion matrices extracted from CapgMyo dataset for DB-a and DB-c are respectively illustrated in Tables 4 and 5. In these experiments, the trained classifier is run 200000 times on DB-a and DB-c database. The confusion matrices compare target and predicted hand gesture classes during the test stage to identify the nature of the classification errors, as well as their quantities. The correct predictions for each output class are bolded in the tables. According to the similarities of the hand gestures, the tables highlight the occurring misclassifications accordingly. For example, in Table 4, class 1 (*Thumb up*) is misclassified 0.43 % as class 6 (*Fingers flexed together in fist*) which is the closest gesture in the dataset compared to class 1. The same applies in Table V, where class 6 (*Ring extension*) is misclassified 3.04 % as class 7 (*Little finger flexion*). Fig.8 illustrates the response time of the proposed hardware classifier for various input window size and hidden neuron ( $N_h$ ). The response time for the employed datasets (DB-a and DB-c) is shown with red square boxes. It should be noted that the proposed architecture can be conveniently modified for larger networks while delivering enough response time.

## 8 Discussion

In this work, we have demonstrated how complex deep learning algorithms can be modified for portable and embedded biomedical applications. By using hardware resource sharing, a flexible and efficient classifier can be delivered where throughput of the system is traded off with hardware complexity and cost. It was also

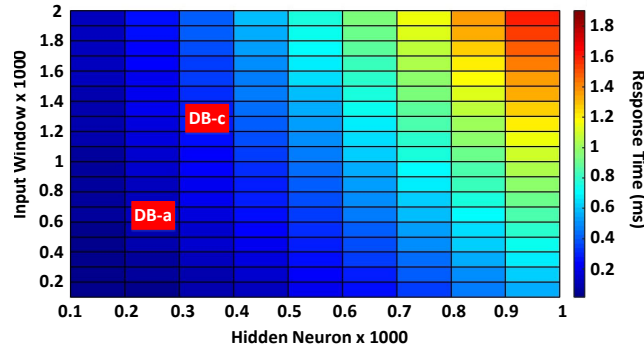


Figure 8: Response time of the proposed hardware classifier for various input window size and hidden neuron ( $N_h$ ). The response time for the employed datasets (DB-a and DB-c) is shown with red square box.

highlighted that such a compromise is only feasible in systems where the underlying time series has slow dynamics, as in the case of physiological systems. Otherwise, the faster the dynamics, the less resource sharing can be exploited. Moreover, for the purpose of performance evaluation, two case studies were investigated and results illustrated acceptable accuracy for both cases. Hardware synthesis and physical implementation also confirmed that the proposed hardware achieved  $1.46\times$  higher GOPs/Slice than similar state of the art FPGA-based accelerators. The proposed hardware architecture may lay the groundwork towards developing a generalized on-chip classifier for wearable biomedical applications where continuous classification on the patient is required such as in seizure detection for epileptic patients or continuous imaging and classification of bladder, liver and heart using ultrasound machines.

## 9 Support Materials

A python code and the corresponding Lorenz training/test data for the results provided in Section 3 are available online at: [https://github.com/hs15/LSTM\\_CLASSIFIER](https://github.com/hs15/LSTM_CLASSIFIER)

## References

- [1] Shyamal Patel, Hyung Park, Paolo Bonato, Leighton Chan, and Mary Rodgers. A review of wearable sensors and systems with application in rehabilitation. *Journal of neuroengineering and rehabilitation*, 9(1):21, 2012.
- [2] Sinziana Mazilu, Ulf Blanke, Michael Hardegger, Gerhard Tröster, Eran Gazit, and Jeffrey M Hausdorff. Gaitassist: a daily-life support and training system for parkinson’s disease patients with freezing of gait. In *Proceedings of the 32nd annual ACM conference on Human factors in computing systems*, pages 2531–2540. ACM, 2014.
- [3] Andreas Bulling, Ulf Blanke, and Bernt Schiele. A tutorial on human activity recognition using body-worn inertial sensors. *ACM Computing Surveys (CSUR)*, 46(3):33, 2014.
- [4] Oscar D. Lara and A. Labrador Miguel. A survey on human activity recognition using wearable sensors. *IEEE Communications Surveys and Tutorials*, 15(3):1192–1209, 2013.
- [5] Yanjun Jia. Dietetic and exercise therapy against diabetes mellitus. In *Second International Conference on Intelligent Networks and Intelligent Systems*, pages 693–696. IEEE, 2009.
- [6] Jie Yin, Yang Qiang, and Junfeng Pan Jeffrey. Sensor-based abnormal human-activity detection. *EEE Transactions on Knowledge and Data Engineering*, 20(8):082–1090, 2009.
- [7] Tesla k80 gpu accelerator. *Board Specification* <https://images.nvidia.com/content/pdf/kepler/Tesla-K80-BoardSpec-07317-001-v05.pdf>, 2015.
- [8] Norman P. Jouppi, Young Cliff, Patil Nishant, Patterson David, Agrawal Gaurav, Bajwa Raminder, Bates Sarah, and et al. In-datacenter performance analysis of a tensor processing unit. *arXiv preprint arXiv:1704.04760*, 2017.
- [9] Intel xeon processor e5–4669 v3. <http://ark.intel.com/products/85766/Intel-Xeon-Processor-E5-4669-v3-45M-Cache-2.10-GHz>, 2016.

- [10] Sepp Hochreiter and Jürgen Schmidhuber. Long short-term memory. *Neural computation*, 9(8):1735–1780, 1997.
- [11] Weidong Geng, Yu Du, Wenguang Jin, Wentao Wei, Yu Hu, and Jiajun Li. Gesture recognition by instantaneous surface emg images. *Scientific reports*, 6:36571, 2016.
- [12] Alex Graves and Schmidhuber Jrgen. Framewise phoneme classification with bidirectional lstm and other neural network architectures. *Neural Networks*, 18(5):602–610, 2005.
- [13] Itay Hubara, Matthieu Courbariaux, Daniel Soudry, Ran El-Yaniv, and Yoshua Bengio. Quantized neural networks: Training neural networks with low precision weights and activations. *arXiv preprint arXiv:1609.07061*, 2016.
- [14] Fengfu Li, Bo Zhang, and Bin Liu. Ternary weight networks. *arXiv preprint arXiv:1605.04711*, 2016.
- [15] Zachary C Lipton, David C Kale, Charles Elkan, and Randall Wetzell. Learning to diagnose with lstm recurrent neural networks. *arXiv preprint arXiv:1511.03677*, 2015.
- [16] Andrej Karpathy. The unreasonable effectiveness of recurrent neural networks. <http://karpathy.github.io/2015/05/21/rnn-effectiveness/>, 2015.
- [17] Robert M May. Simple mathematical models with very complicated dynamics. *Nature*, 261(5560):459–467, 1976.
- [18] Edward N Lorenz. Deterministic nonperiodic flow. *Journal of the atmospheric sciences*, 20(2):130–141, 1963.
- [19] John Duchi, Elad Hazan, and Yoram Singer. Adaptive subgradient methods for online learning and stochastic optimization. *Journal of Machine Learning Research*, 12(Jul):2121–2159, 2011.
- [20] Murugan Sankaradas, Venkata Jakkula, Srihari Cadambi, Srimat Chakradhar, Igor Durdanovic, Eric Cosatto, and Hans Peter Graf. A massively parallel coprocessor for convolutional neural networks. In *Application-specific Systems, Architectures and Processors, 2009. ASAP 2009. 20th IEEE International Conference on*, pages 53–60. IEEE, 2009.
- [21] Mohammad Motamedi, Philipp Gysel, Venkatesh Akella, and Soheil Ghiasi. Design space exploration of fpga-based deep convolutional neural networks. In *Design Automation Conference (ASP-DAC), 2016 21st Asia and South Pacific*, pages 575–580. IEEE, 2016.
- [22] Jiantao Qiu, Jie Wang, Song Yao, Kaiyuan Guo, Boxun Li, Erjin Zhou, Jincheng Yu, Tianqi Tang, Ningyi Xu, Sen Song, et al. Going deeper with embedded fpga platform for convolutional neural network. In *Proceedings of the 2016 ACM/SIGDA International Symposium on Field-Programmable Gate Arrays*, pages 26–35. ACM, 2016.
- [23] Haruyoshi Yonekawa and Hiroki Nakahara. On-chip memory based binarized convolutional deep neural network applying batch normalization free technique on an fpga. In *Parallel and Distributed Processing Symposium Workshops (IPDPSW), 2017 IEEE International*, pages 98–105. IEEE, 2017.